LIVERPOOL JOHN MOORES UNIVERSITY

LJMU Research Online

Levi, E, Brkovic, B, Jecmenica, M and Lazarevic, Z

Saturated VSD model of a six-phase induction machine

http://researchonline.ljmu.ac.uk/id/eprint/13891/

Article

Citation (please note it is advisable to refer to the publisher's version if you intend to cite from this work)

Levi, E, Brkovic, B, Jecmenica, M and Lazarevic, Z Saturated VSD model of a six-phase induction machine. IET Electric Power Applications. ISSN 1350-2352 (Accepted)

LJMU has developed **LJMU Research Online** for users to access the research output of the University more effectively. Copyright © and Moral Rights for the papers on this site are retained by the individual authors and/or other copyright owners. Users may download and/or print one copy of any article(s) in LJMU Research Online to facilitate their private study or for non-commercial research. You may not engage in further distribution of the material or use it for any profit-making activities or any commercial gain.

The version presented here may differ from the published version or from the version of the record. Please see the repository URL above for details on accessing the published version and note that access may require a subscription.

For more information please contact researchonline@ljmu.ac.uk

http://researchonline.ljmu.ac.uk/

LIVERPOOL JOHN MOORES UNIVERSITY

LJMU Research Online

Levi, E, Brkovic, B, Jecmenica, M and Lazarevic, Z

Saturated VSD model of a six-phase induction machine

http://researchonline.ljmu.ac.uk/id/eprint/13891/

Article

Citation (please note it is advisable to refer to the publisher's version if you intend to cite from this work)

Levi, E, Brkovic, B, Jecmenica, M and Lazarevic, Z Saturated VSD model of a six-phase induction machine. IET Electric Power Applications. ISSN 1350-2352 (Accepted)

LJMU has developed **LJMU Research Online** for users to access the research output of the University more effectively. Copyright © and Moral Rights for the papers on this site are retained by the individual authors and/or other copyright owners. Users may download and/or print one copy of any article(s) in LJMU Research Online to facilitate their private study or for non-commercial research. You may not engage in further distribution of the material or use it for any profit-making activities or any commercial gain.

The version presented here may differ from the published version or from the version of the record. Please see the repository URL above for details on accessing the published version and note that access may require a subscription.

For more information please contact researchonline@ljmu.ac.uk

http://researchonline.ljmu.ac.uk/

IET Research Journals

Submission Template for IET Research Journal Papers

IET Journals
The Institution of Engineering and Technology

ISSN 1751-8644
doi: 0000000000
www.ietdl.org

Saturated VSD model of a six-phase induction machine

Bogdan Brkovic[1*], *Milos Jecmenica*[1], *Emil Levi*[2], *Zoran Lazarevic*[1]

[1] *Faculty of Electrical Engineering, University of Belgrade, Bulevar Kralja Aleksandra 73, 11000 Belgrade, Serbia*
[2] *Department of Electronics and Electrical Engineering, Liverpool John Moores University, Byrom Street, Liverpool L3 3AF, UK*
** E-mail: brkovic@etf.bg.ac.rs*

Abstract: In this paper, a saturated model of an asymmetrical six-phase induction machine is presented. The model is based on the vector space decomposition approach, and it includes main and leakage flux saturation, as well as the mutual coupling between orthogonal planes, while using the Gamma equivalent circuit approach. The accuracy of the proposed model in unbalanced operating modes that are characteristic for multiphase machines, such as post-fault and power sharing operation, makes it advantageous compared to existing models. The model is developed assuming that the machine operates in asymmetrical conditions and that, therefore, there is fundamental frequency excitation in both planes. The inter-plane coupling effect is examined using finite element analysis and an experimental procedure for its quantification is developed. The model is verified by comparison with the experimental results obtained from a prototype asymmetrical six-phase induction machine, and its advantages compared to existing models are emphasized.

1 Introduction

Multiphase electrical machines are an opportune choice for a wide range of applications in modern power systems, such as high-power industrial drives [1], electric vehicles [2], more-electric aircraft [3, 4], and wind energy conversion [5]. Multiphase machines exhibit multiple advantages compared to their traditionally employed three-phase counterparts, the most noteworthy being increased torque density and torque/current ratio, reduced torque ripple, improved fault tolerance and lower current harmonic distortion [1, 6, 7].

Accurate modelling and parameter determination are essential for proper control and performance analysis of multiphase machines [8]. A straightforward approach would be to model the multiphase machine using phase-domain variables. However, the phase-variable model is highly computationally demanding due to time-varying inductance matrix coefficients [9]. This led to the development of alternative modelling approaches: the multiple dq [10], vector space decomposition (VSD) [11] and voltage behind reactance (VBR) [12] models. Each approach is more or less beneficial depending on the intended application.

Regardless of the model employed, proper modelling of magnetic circuit saturation is required for achieving satisfactory simulation accuracy and control performance. Electrical machines usually operate in the saturated region to increase torque density [13]. Extensive research was devoted to saturated models of three-phase machines over the past decades and is well documented [14–17]. Saturated multiphase machine models are still under development, with some notable research reported in [12, 18–21]. Most of the available models rely on including only main flux saturation, which relates directly to existing saturated three-phase machine models. Specific aspects of saturation in five-phase machines regarding the air-gap flux waveform have been studied in depth in [22] and [12].

In recent years, the VSD model has been a preferred choice for the control of multiphase machines [23–25]. However, an in-depth study of the saturation influence on the VSD model remains to be conducted. A coupling effect between the orthogonal subspaces (planes) of an asymmetrical six-phase induction machine (6PIM) was observed and described in [26]. This effect was termed "interplane cross-saturation", or IPCS for short. This phenomenon represents a mutual coupling between fundamental frequency quantities of the dq and xy planes. In normal operating conditions there are no fundamental currents in the xy plane. Fundamental frequency components in the xy plane are related to unbalanced operation, and therefore need to be accounted for in fault-tolerant control [25, 27] and arbitrary power-sharing algorithms for multiple three-phase winding machines [28, 29]. Saturated multiphase machine models which include the mutual influence between the dq and xy plane have been reported in literature [12], but only the influence of higher-order xy current harmonics was studied, which is not applicable for analysing unbalanced operation. This imposes the need to develop a new VSD model including the IPCS effect.

In this paper, the VSD model of a 6PIM with a distributed winding (shown in the Appendix, subsection 8.1), including main and leakage flux saturation, as well as the IPCS effect is presented. A parameter measurement procedure for determining the coupling flux components due to IPCS is developed. The proposed model provides improved accuracy compared to existing models when analysing unbalanced operating modes with pronounced saturation. The model validity and parameter measurement accuracy are verified experimentally. Verification is performed for operating modes with pronounced saturation and voltage unbalance.

This paper is organized as follows. The conventional linear VSD model is presented in section 2. The VSD model is formulated using a Gamma equivalent circuit in section 3. The development of the model including main flux saturation and IPCS is presented in the fourth section. The parameter measurement procedure and a comparison between simulation results and experimental results are given in section 5. The final section summarises the conclusions of the presented research.

2 Conventional VSD model

The VSD model voltage equations of a 6PIM in the dq and xy plane are given in space-vector form as follows [9]:

$$\vec{u}_{dqs} = R_s\vec{i}_{dqs} + \frac{d\vec{\psi}_{dqs}}{dt} + \mathrm{j}\omega_e\vec{\psi}_{dqs} \tag{1a}$$

$$\vec{u}_{dqr} = R_r\vec{i}_{dqr} + \frac{d\vec{\psi}_{dqr}}{dt} + \mathrm{j}(\omega_e - \omega_r)\vec{\psi}_{dqr} \tag{1b}$$

$$\vec{u}_{xys} = R_s\vec{i}_{xys} + \frac{d\vec{\psi}_{xys}}{dt}, \tag{1c}$$

This paper is a postprint of a paper submitted to and accepted for publication in [journal] and is subject to Institution of Engineering and Technology Copyright. The copy of record is available at the IET Digital Library.

where ω_r (rad/s) is the rotor electrical angular speed, and ω_e (rad/s) is the arbitrary angular speed of the rotating reference frame. Note that the zero-sequence equations are excluded from the given model, due to the fact that the neutral points of the 6PIM are considered isolated in the upcoming analyses. The machine could of course be configured with a single neutral point, in which case injection of the third stator harmonic current would be possible. This would undoubtedly impact significantly on the saturation-related behaviour of the machine. However, configuration with single neutral and the third harmonic stator current injection for torque enhancement purposes is never used in practice since it requires the connection of the machine's neutral point to either a seventh inverter leg or a midpoint of the dc-link capacitor bank [30, 31]. Hence this situation is not considered in the paper.

Additionally, since a machine with a squirrel-cage rotor is used, the rotor voltages are set to zero further on. The space vectors in the dq and xy subspaces are defined as:

$$\vec{\xi}_{dqs} = \xi_{ds} + \mathrm{j}\xi_{qs} \tag{2a}$$

$$\vec{\xi}_{dqr} = \xi_{dr} + \mathrm{j}\xi_{qr} \tag{2b}$$

$$\vec{\xi}_{xys} = \xi_{xs} + \mathrm{j}\xi_{ys}, \tag{2c}$$

where ξ stands for an arbitrary 6PIM electrical quantity (voltage, current, or flux linkage). The flux linkages are given as:

$$\vec{\psi}_{dqs} = (L_m + L_{lsdq})\vec{i}_{dqs} + L_m\vec{i}_{dqr} \tag{3a}$$

$$\vec{\psi}_{dqr} = (L_m + L_{lr})\vec{i}_{dqr} + L_m\vec{i}_{dqs} \tag{3b}$$

$$\vec{\psi}_{xys} = L_{xy}\vec{i}_{xys}, \tag{3c}$$

where L_m is the magnetizing inductance, L_{lsdq} is the stator leakage inductance in the dq plane, and L_{xy} is the stator leakage inductance in the xy plane. The leakage inductances in the dq and xy planes are generally not equal due to mutual leakage inductance, as elaborated in [32]. Note that there is no mutual influence between the quantities of different subspaces, and that, with no saturation involved, all inductances in (3) are constant. The electromagnetic torque equation is given as:

$$T_e = \frac{1}{3K^2} p \,\mathrm{Im}\left(\vec{\psi}_{dqs} \cdot \vec{i}^{\,*}_{dqr}\right) \tag{4}$$

where $*$ denotes complex conjugation, p is the pole pair number, and K is the VSD transformation coefficient. The value of K can be chosen arbitrarily, and is set to $K = 1/3$ in all the analyses in this paper, thereby keeping the peak values of electrical quantities from the original phase-variable reference frame invariant. To complete the model, the electromechanical motion equation needs to be included:

$$T_e - T_L = J\frac{d\Omega}{dt} + k_f\Omega, \tag{5}$$

where T_L is the load torque, J is the moment of inertia, $\Omega = \omega/p$ is the mechanical angular rotor speed, and k_f is the friction coefficient.

3 Gamma model

As Slemon demonstrated in [33], the Gamma (Γ) model is a suitable alternative to the conventional T-form model of a three-phase induction machine. In fact, the Γ model was shown to be advantageous in terms of including main flux saturation in motoring mode, when saturation occurs dominantly in the stator magnetic circuit. An obvious advantage of the Γ model is that the equivalent circuit parameters may be obtained directly from the conventional no-load and locked-rotor tests.

The 6PIM equations in the dq plane are identical to those of the dq model of a three-phase induction machine. This allows the dq subspace to be modelled using the Γ circuit. The T and Γ equivalent circuits corresponding to the stationary reference frame ($\omega_e = 0$) are displayed in Fig. 1. The rotor quantities of the Γ model are related to those of the T model as follows:

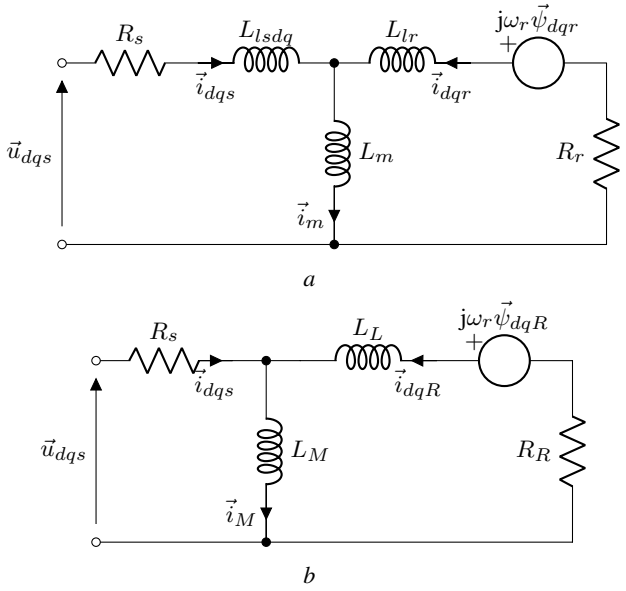

Fig. 1: Equivalent circuits of a 6PIM in the dq plane in the stationary reference frame
a T circuit
b Γ circuit

$$\vec{\psi}_{dqR} = \gamma\vec{\psi}_{dqr} \tag{6a}$$

$$\vec{i}_{dqR} = \frac{\vec{i}_{dqr}}{\gamma}, \tag{6b}$$

where $\gamma = L_s/L_m$ and $L_s = L_m + L_{lsdq}$ is the stator no-load inductance. The relationships between Γ and T circuit parameters are given as:

$$L_M = \gamma L_m = L_s \tag{7a}$$

$$L_L = \gamma L_{lsdq} + \gamma^2 L_{lr} \tag{7b}$$

$$R_R = \gamma^2 R_r. \tag{7c}$$

All parameters of the Γ circuit can be obtained directly from the standard no-load and locked-rotor tests under dq voltage supply. The stator resistance can be determined either from the DC test or the xy sequence test [34]. The inductance L_M, which will be referred to as the "magnetizing inductance" further on, is equal to the no-load inductance, and is therefore obtained from the no-load test. After this, the locked-rotor test enables the determination of the two remaining parameters – the leakage inductance L_L and the rotor resistance R_R. Note that the coefficient γ can only be determined provided that the magnetizing inductance is known. However, this information is only required if the values of actual rotor quantities are of interest, which is usually not the case.

The Γ model is used in all of the following analyses. The dq plane equations of the conventional VSD model given in the previous section should be appropriately modified. The model in the xy subspace remains unaltered, as the Γ model relates only to the dq quantities. The voltage equations (1) and the torque equation (4) retain the same form, except that the indices "r" should be replaced with "R" in all instances. The rotor voltage equation is now given as:

$$0 = R_R\vec{i}_{dqR} + \frac{d\vec{\psi}_{dqR}}{dt} + \mathrm{j}(\omega_e - \omega_r)\vec{\psi}_{dqR}, \tag{8}$$

whereas the torque equation is given as:

$$T_e = \frac{1}{3K^2} p \,\mathrm{Im}\left(\vec{\psi}_{dqs} \cdot \vec{i}^{\,*}_{dqR}\right) \tag{9}$$

© The Institution of Engineering and Technology 2015

The flux equations of the linear Γ model are given as follows:

$$\vec{\psi}_{dqs} = L_M \left(\vec{i}_{dqs} + \vec{i}_{dqr} \right) \tag{10a}$$

$$\vec{\psi}_{dqR} = L_M \left(\vec{i}_{dqs} + \vec{i}_{dqr} \right) + L_L \vec{i}_{dqR}. \tag{10b}$$

4 Proposed saturated VSD model

According to the results of [26], the dq and xy planes are coupled under saturated conditions. This phenomenon has been termed interplane cross-saturation. In the following subsections, a detailed analysis of IPCS and its effect on model variables is carried out using Finite element analysis (FEA). After that, a new model is proposed, incorporating main flux saturation and IPCS effect. Therein, the linear Γ model presented in section 3 is used as a foundation.

4.1 Finite element analysis of IPCS

The goal of this analysis is to determine the influence of IPCS on the flux linkages in the dq and xy planes. This is achieved by comparing the flux linkages obtained when only the current components in the corresponding plane exist to those obtained when current components in both planes are present. In other words, the difference between the flux linkage values corresponding to cases with and without mutual interaction between the orthogonal planes needs to be determined. These differences are expressed as:

$$\Delta\vec{\psi}_{dq}(\hat{i}_M, \hat{i}_{xys}) = \vec{\psi}_{dqs}(\hat{i}_M, \hat{i}_{xys}) - \vec{\psi}_{dqs}(\hat{i}_M, 0) \tag{11a}$$

$$\Delta\vec{\psi}_{xy}(\hat{i}_M, \hat{i}_{xys}) = \vec{\psi}_{xys}(\hat{i}_M, \hat{i}_{xys}) - \vec{\psi}_{xys}(0, \hat{i}_{xys}), \tag{11b}$$

where $\Delta\vec{\psi}_{dq}$ and $\Delta\vec{\psi}_{xy}$ are the flux changes caused by IPCS, and $\hat{i}_M$ and $\hat{i}_{xys}$ represent the magnitudes of the magnetizing and xy plane space vectors, respectively. It should be noted that the FEA was conducted under conditions corresponding to no-load operation, hence the $\hat{i}_M$ is equivalent to the magnitude of the dq plane current space vector, i.e. $\hat{i}_M \equiv \hat{i}_{dqs}$.

The FE simulations were executed for multiple combinations of dq and xy currents, and the flux linkage changes attributed to IPCS were determined according to (11) for each combination. The machine model used in the FEA is based on the actual 6PIM prototype used in the upcoming experimental investigation. The construction details (machine dimensions and winding data) and rated data of the prototype are given in subsection 8.1 of the Appendix. Details regarding the FE model and an example of an FEA solution with the displayed finite element mesh and flux density distribution are also given in the Appendix, in subsection 8.2. In order to determine the dependence of the flux increments on the dq and xy current components, the FEA is performed for the following scenarios:

1. phase currents exciting only the dq subsystem are assigned to the windings (flux linkages $\vec{\psi}_{dqs}(\hat{i}_M, 0)$ and $\vec{\psi}_{xys}(\hat{i}_M, 0)$ are obtained);
2. phase currents exciting only the xy subsystem are assigned to the windings (flux linkages $\vec{\psi}_{dqs}(0, \hat{i}_{xys})$ and $\vec{\psi}_{xys}(0, \hat{i}_{xys})$ are obtained);
3. all combinations of phase currents from scenarios 1 and 2 are assigned to the windings, thereby exciting both the dq and xy subsystems (flux linkages $\vec{\psi}_{dqs}(\hat{i}_M, \hat{i}_{xys})$ and $\vec{\psi}_{xys}(\hat{i}_M, \hat{i}_{xys})$ are obtained).

Each step of the analysis is conducted as follows:

- the values of currents in the dq and xy subspace ($\hat{i}_M$ and $\hat{i}_{xys}$) are selected;
- the phase current values to be assigned to the windings are calculated by applying the inverse VSD transformation [9] to the dq and xy current components;
- the FE simulation is conducted for the assigned current values and the values of per-phase flux linkages are obtained;
- the complex VSD transformation is applied to the per-phase flux linkages values to obtain the space vectors of flux linkages in the dq and xy subspace $\vec{\psi}_{dqs}$ and $\vec{\psi}_{xys}$.

The described procedure is repeated for all three scenarios, with $\hat{i}_M$ and $\hat{i}_{xys}$ ranging from 0 to 6 A. The flux linkage changes are then determined by applying (11a) and (11b). The obtained flux changes were found to be shifted by approximately 180° with respect to the total flux linkages, and can therefore be expressed as follows (the negative sign is incorporated in the amplitudes of the flux increments):

$$\Delta\vec{\psi}_{dq}(\hat{i}_M, \hat{i}_{xys}) = \Delta\psi_{dq}(\hat{i}_M, \hat{i}_{xys}) \mathrm{e}^{\mathrm{j}\angle\vec{\psi}_{dqs}} \tag{12a}$$

$$\Delta\vec{\psi}_{xy}(\hat{i}_M, \hat{i}_{xys}) = \Delta\psi_{xy}(\hat{i}_M, \hat{i}_{xys}) \mathrm{e}^{\mathrm{j}\angle\vec{\psi}_{xys}}, \tag{12b}$$

where $\Delta\psi_{dq}$ and $\Delta\psi_{xy}$ are algebraic values of the flux changes. The computed values are displayed in Fig. 2. The presented results clearly demonstrate that the flux changes are negative, i.e. that the IPCS effect causes a reduction of flux linkage values in both planes. Considering the flux values in the corresponding planes (rated dq plane flux ~ 0.7 Wb; xy plane flux at rated current ~ 35mWb), the IPCS effect is much more pronounced in the xy plane than in the dq plane. This can be attributed to the main flux saturation, which has a much greater influence on the dq plane flux linkage compared to IPCS, particularly at large values of magnetizing current, as will be demonstrated next.

The main flux saturation may be accounted for by expressing the magnetizing flux as a non-linear function of the magnetizing current:

$$\vec{\psi}_M(\hat{i}_M) = \vec{\psi}_{Mu} + \Delta\psi_M(\hat{i}_M) \mathrm{e}^{\mathrm{j}\angle\vec{\psi}_M}, \tag{13}$$

where $\vec{\psi}_{Mu} = L_{Mu}\vec{i}_M$ is the unsaturated value of magnetizing flux linkage, L_{Mu} is the unsaturated value of the magnetizing inductance and $\Delta\psi_M$ is the algebraic flux change due to main flux saturation. According to the Γ model relationships, it follows that $\vec{\psi}_M \equiv \vec{\psi}_{dqs}$ and $\Delta\vec{\psi}_M \equiv \Delta\vec{\psi}_{dqs}$, i.e. the value $\Delta\psi_M$ actually represents the change in the dq plane flux linkage. This allows the total difference between the values of actual and unsaturated dq plane flux linkages to be expressed as:

$$\begin{aligned} \Delta\vec{\psi}'_{dq}(\hat{i}_M, \hat{i}_{xys}) &= \Delta\vec{\psi}_M(\hat{i}_M) + \Delta\vec{\psi}_{dq}(\hat{i}_M, \hat{i}_{xys}) \\ &= \left[\Delta\psi_M(\hat{i}_M) + \Delta\psi_{dq}(\hat{i}_M, \hat{i}_{xys}) \right] \mathrm{e}^{\mathrm{j}\angle\vec{\psi}_{dqs}}. \end{aligned} \tag{14}$$

The values of $\Delta\psi'_{dq}$ obtained from FE simulations are displayed in Fig. 3. By comparing Figs. 2*a* and 3, it can be observed that the contribution of main flux saturation exceeds that of IPCS by up to two orders of magnitude. This indicates that the influence of IPCS on the dq plane flux linkage can be neglected from a practical standpoint. This possibility will be re-evaluated after obtaining the experimental results.

4.2 Model formulation

Based on the results obtained in the previous subsection, a saturated model of a 6PIM is proposed. The new model is based on the Γ model presented in section 3. Flux linkages in the dq and xy planes are used as the state variables. The flux equations in the dq and xy subspaces need to be modified in order to model the IPCS effect and main flux saturation. The following form of the flux equations is proposed:

$$\vec{\psi}_{dqs} = L_{Mu}\vec{i}_M + \Delta\vec{\psi}'_{dq}(\hat{i}_M, \hat{i}_{xys}) \tag{15a}$$

$$\vec{\psi}_{dqR} = L_{Mu}\vec{i}_M + \Delta\vec{\psi}'_{dq}(\hat{i}_M, \hat{i}_{xys}) + L_L\vec{i}_{dqR} \tag{15b}$$

$$\vec{\psi}_{xys} = L_{xy}\vec{i}_{xys} + \Delta\vec{\psi}_{xy}(\hat{i}_M, \hat{i}_{xy}). \tag{15c}$$

© The Institution of Engineering and Technology 2015

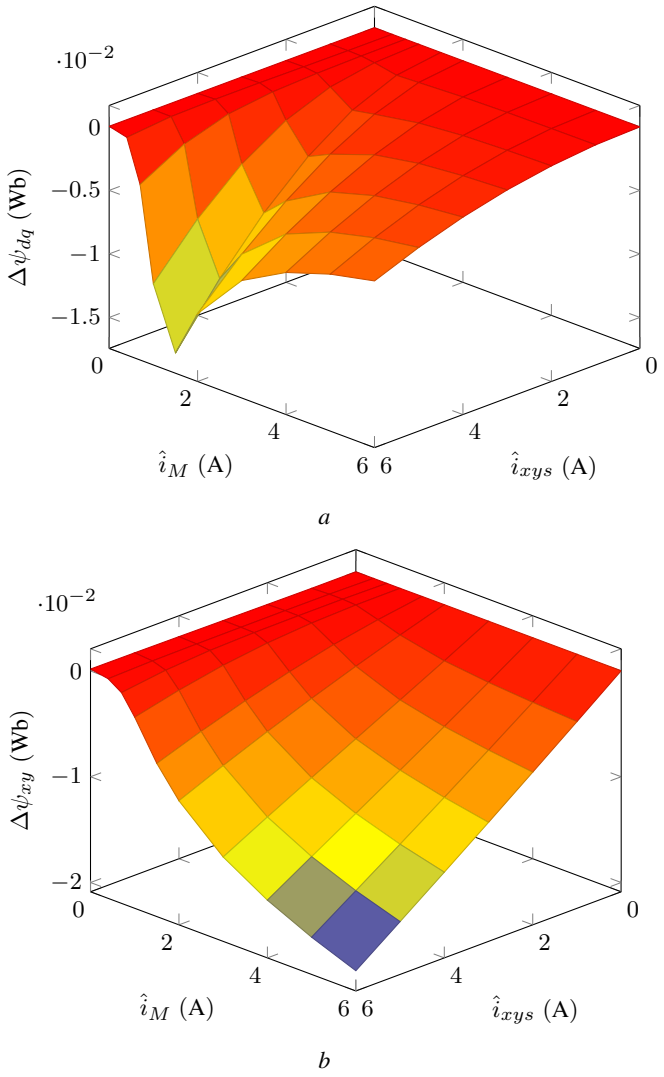

Fig. 2: Changes of flux linkages due to IPCS determined by FEA
a flux change in the dq plane
b flux change in the xy plane

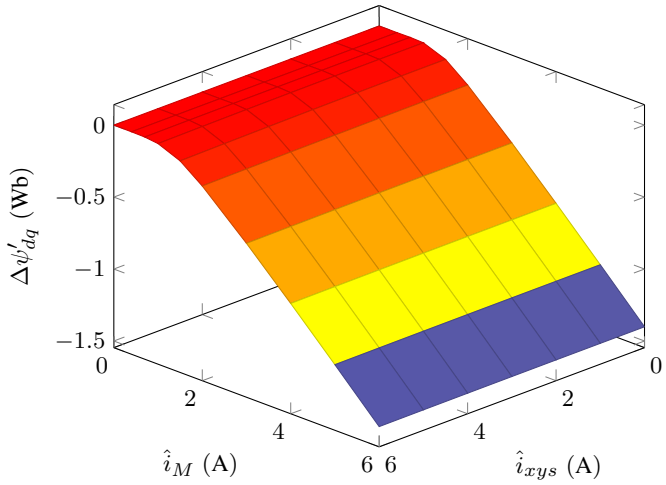

Fig. 3: Total change of dq plane flux linkage due to IPCS and main flux saturation determined by FEA

The voltage, torque and electromechanical motion equations remain unaltered compared to the original linear model. The following equations constitute the saturated 6PIM VSD model:

- voltage equations (1a), (8), and (1c),
- flux-current relationships (15),
- algebraic torque equation (9), and
- electromechanical motion equation (5).

The listed equations form a set of non-linear differential-algebraic equations (DAE), which can be readily solved by appropriate numerical integration methods. The non-linear flux increments can be included in the model by means of either lookup tables or suitable analytical functions.

5 Experimental results and discussion

5.1 Experimental setup overview

The experimental assembly used for 6PIM testing is depicted in Fig. 4. The core component is the 6PIM prototype, constructed by rewinding a three-phase squirrel-cage induction machine. As stated in section 4.1, the rated data and construction parameters of the prototype are given in the Appendix. The 6PIM is supplied from two identical converter groups, each comprised of an input rectifier stage, DC link, and an output inverter stage. The 6PIM is operated with two isolated neutrals.

Motor currents are measured using six LEM current sensors, and the DC link voltage of the converters is measured using a high-voltage sensing board with input-output isolation and differential outputs. Converter control and analog-to-digital conversion (ADC) of measured signals are performed using the Power Electronics and Drives Board (PED-Board for short) controller based on an sbRIO-9651 platform by National Instruments. The sbRIO system incorporates an FPGA and processor, which allows simultaneous execution of multiple processes at various sampling rates. The PWM signal generation and high-speed A/D conversion are implemented on the FPGA, whereas the reference voltage values and other commands are executed via the processor. Sampled data are buffered and transferred to the PC for visualization and logging purposes, given the limited memory capacity of the FPGA and processor. The complete converter control and data acquisition algorithm was developed using the NI LabVIEW software package.

The converters are voltage controlled (open-loop control), and conventional (carrier-based) PWM is used. The switching period is set to 120 μs, with the inverter dead-time of 4.3 μs. The ADC sampling rate is set to 40 kHz. The measured signals are pre-filtered in order to avoid aliasing. Dead-time compensation is applied to the reference voltages, thereby eliminating the requirement for voltage measurement [35].

5.2 Parameter determination

The model parameters that need to be identified are: stator and rotor resistances (R_s, R_R), leakage inductances in the dq and xy plane (L_L, L_{xy}), unsaturated magnetizing inductance (L_{Mu}), and flux changes due to main flux saturation and IPCS ($\Delta\psi'_{dq}$, $\Delta\psi_{xy}$). The stator resistance and leakage inductance in the xy plane are determined from the xy sequence test, as described in [32, 34]. The unsaturated magnetizing inductance, dq plane leakage inductance and rotor resistance are determined from the standard no-load and locked-rotor tests. The rotating speed of the 6PIM is maintained equal to synchronous speed by means of an auxiliary three-phase induction machine during the no-load and xy sequence tests.

The values of leakage inductances in the dq and xy subspaces are plotted against corresponding current magnitudes and displayed in Fig. 5. Both inductances are current-dependant, especially the one in the dq plane. This can be attributed to immediate saturation of rotor slot openings even at low current values, which is typical in the case of closed rotor slot [36]. This effect is very pronounced and needs to be accounted for. According to the guidelines for including leakage flux saturation given in [33], L_L is expressed as a non-linear function of $\hat{i}_{dqs}$ (see the Appendix, subsection 8.3). The non-linearity of the xy plane inductance need not be explicitly modelled, but rather appended to the $\Delta\psi_{xy}$ term, as demonstrated later in this section. It

© The Institution of Engineering and Technology 2015

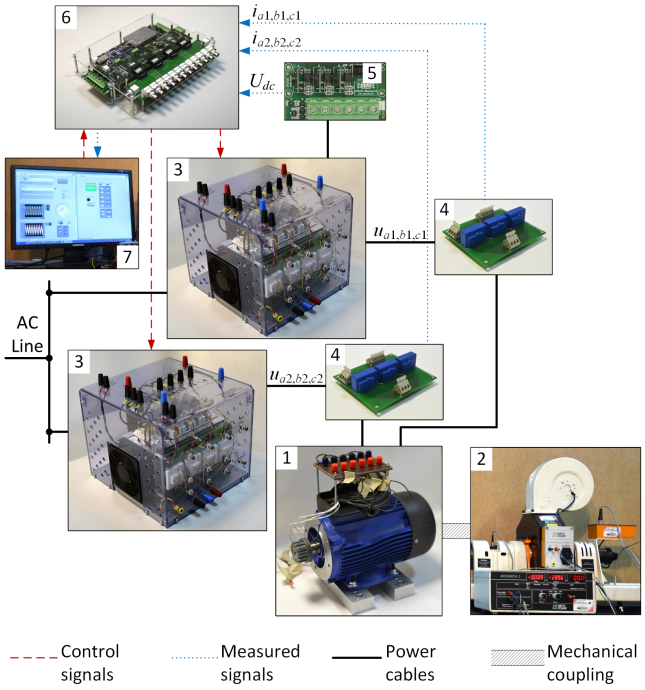

Fig. 4: Layout of the experimental setup: 1 – 6PIM, 2 – magnetic powder brake (load), 3 – three-phase AC-DC-AC converter, 4 – LEM sensors for measuring 6PIM phase currents, 5 – high-voltage sensing board for measuring DC link voltage, 6 – PED-Board controller for converter control and signal acquisition, 7 – PC

should be noted that the FEM results did not reveal non-linear phenomena in the xy plane aside from those related to IPCS, i.e. the xy plane inductance was constant. This is the consequence of insufficient information regarding the machine's magnetic circuit design. The values of resistances and unsaturated inductances are given in Table 1. The table also contains values of magnetizing current, flux and inductance corresponding to no-load operation at rated voltage. These values are denoted $\hat{i}_{Ms}$, $\hat{\psi}_{Ms}$ and $\hat{L}_{Ms}$, respectively, where the index s stands for "saturated".

Table 1 6PIM parameter values

Parameter	Units	Value
L_{Mu}	mH	296
$\hat{i}_{Ms}$	A	2.4
$\hat{\psi}_{Ms}$	Wb	0.51
L_{Ms}	mH	210
L_{Lu}	mH	158
L_{xyu}	mH	14.1
R_s	Ω	2.27
R_R	Ω	1.83

Due to the IPCS effect, additional tests are needed for determining the corresponding flux changes in the dq and xy plane. The experimental procedure for obtaining these values is similar to that applied in the FE analysis of section 4.1. The values of dq and xy plane current components are adjusted to achieve different operating points. The motor is rotated at synchronous speed at all times during the test, hence it can be considered that $\vec{i}_{dqs} \equiv \vec{i}_M$. For each combination of currents, dq and xy plane flux linkage values are calculated

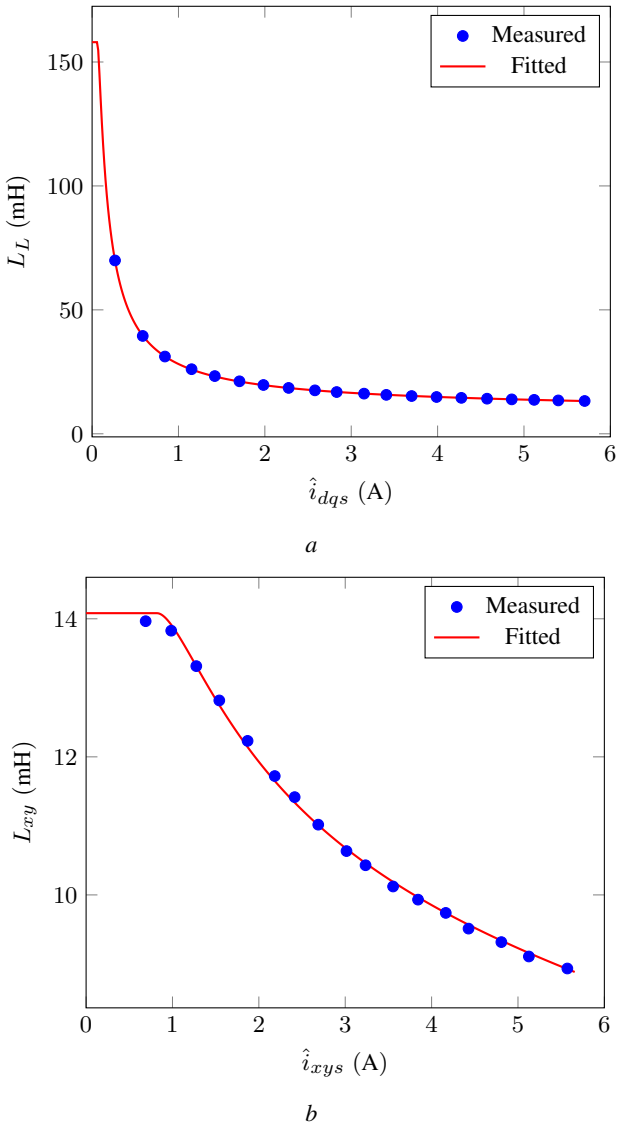

Fig. 5: Experimentally identified leakage inductances. The fitted values are obtained by curve fitting the measured values
a dq plane leakage inductance
b xy plane leakage inductance

as follows:

$$\vec{\psi}_{dqs} = \int \left(\vec{u}_{dqs} - R_s \vec{i}_{dqs} \right) dt \tag{16a}$$

$$\vec{\psi}_{xys} = \int \left(\vec{u}_{xys} - R_s \vec{i}_{xys} \right) dt \tag{16b}$$

After the flux linkages have been determined for all $(\hat{i}_M, \hat{i}_{xys})$ combinations, the flux changes can be determined as described in section 4.1. However, in order to include the saturation of the xy plane inductance, the expression for the flux change in the xy plane needs to be modified. The total change of xy plane flux linkage with respect to its unsaturated value is expressed as follows:

$$\Delta\vec{\psi}'_{xy}(\hat{i}_M, \hat{i}_{xys}) = \vec{\psi}_{xys}(\hat{i}_M, \hat{i}_{xys}) - L_{xyu}\vec{i}_{xys}, \tag{17}$$

where L_{xyu} denotes the unsaturated value of the xy plane inductance. The flux change calculated by (17) includes the IPCS effect and the saturation caused solely by the xy plane current. The flux change in the dq plane is calculated according to (14).

The experimentally identified flux changes are presented in Figs. 6 and 7. Note that the blue dots in the figures represent the

© The Institution of Engineering and Technology 2015

values obtained from measurements, whereas the surfaces represent the interpolated values. The dq plane flux change caused by IPCS alone is displayed in Fig. 6. The experimental values are comparable to the FEM results shown in Fig. 2*a*. The total dq plane flux change displayed in Fig. 7*a* corresponds to the FEM results displayed in Fig. 3. As previously stated, the xy plane saturation observed from the experimental results was not present in the FEM model. Therefore, it can be considered that $\Delta\psi_{xy} \approx \Delta\psi'_{xy}$ in terms of the FEM model, and the xy plane flux change shown in Fig. 7*b* can be related to Fig. 2*b*. The measurement results are fitted by appropriate analytical functions of $(\hat{i}_M, \hat{i}_{xys})$ given in the Appendix (subsection 8.3). These functions are included in flux equations (15). Note that the xy flux linkage equation (15c) should now be rewritten as:

$$\vec{\psi}_{xys} = L_{xyu}\vec{i}_{xys} + \Delta\vec{\psi}'_{xy}(\hat{i}_M, \hat{i}_{xys}), \tag{18}$$

which is actually an alternative formulation of (17).

The presented results confirm the conclusions regarding IPCS derived in section 4.1. It was therein assumed that the influence of the xy current component on the flux change in the dq plane can be neglected from a practical standpoint. The experimental results validate this assumption, as the flux change in the dq plane caused solely by IPCS was determined to be lower than the flux change due to main flux saturation by at least two orders of magnitude at each operating point. Therefore, it is sufficiently accurate to treat $\Delta\psi'_{dq}$ as a function of the magnetizing current alone, as given in the Appendix (subsection 8.3).

5.3 Experimental verification of the model

Based on the results of the FE analysis and the experimental parameter determination, a complete VSD model of the 6PIM including main flux saturation, leakage flux saturation, and IPCS effect, can be formed. The model equations are summarized as follows:

- voltage equations (1a), (8), (1c);
- flux-current relationships (15a), (15b), (18);
- torque equation (9);
- motion equation (5).

The 6PIM parameters are summarized in Table 1, and the non-linear flux changes and inductances are expressed by analytical functions given in the Appendix.

The proposed model was implemented in *Matlab* environment. To enable more efficient simulation of stationary regimes, the steady-state model was formed as well. The dynamic model equations are solved using integrated *Matlab* functions for numerical integration

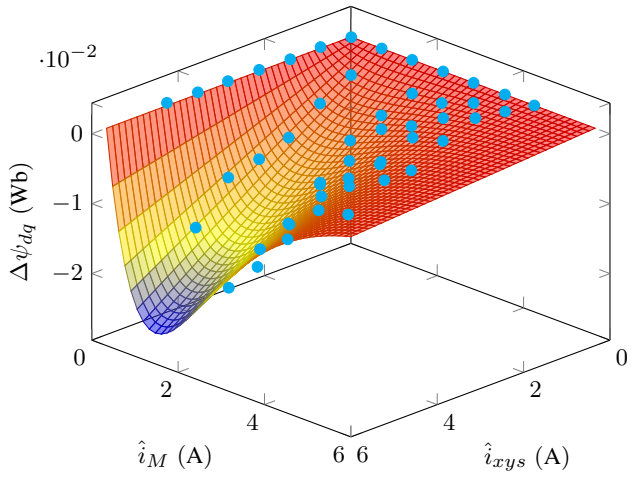

Fig. 6: Experimentally identified dq plane flux change due to IPCS. The surface is obtained by fitting the experimental values, which are represented by the blue dots

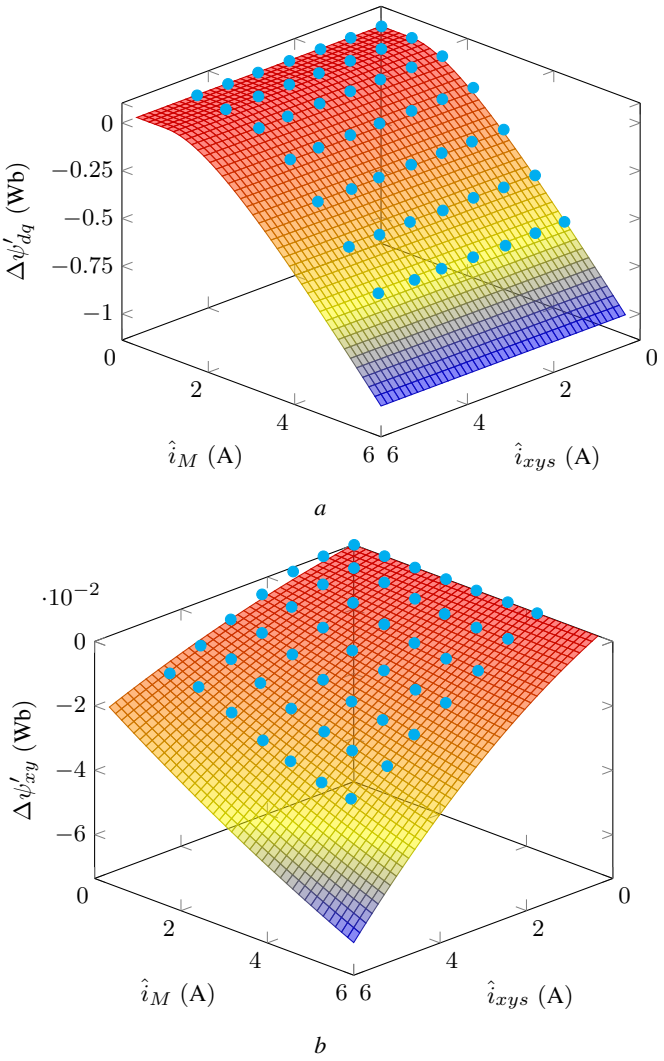

Fig. 7: Experimentally identified total flux changes due to main flux saturation and IPCS. The surfaces are obtained by fitting the experimental values, which are represented by the blue dots
a flux change in the dq plane
b flux change in the xy plane

of DAEs, whereas the steady state model was solved using non-linear algebraic equation solvers. Operating modes with pronounced main flux saturation and unbalanced voltage supply were simulated, in order to emphasize the advantages of the new model compared to existing models. The results of the new model, referred to as the "IPCS model" further on, are compared to the results of the linear VSD model presented in section 3 and the model which includes main and leakage flux saturation, but ignores the IPCS effect. The latter will be referred to as the "saturated VSD model". The linear model uses the constant value of magnetizing inductance equal to L_{Ms} (see Table 1) and the leakage inductance corresponding to rated current.

The steady state model was solved for different values of speed, i.e. mechanical load. First, the experiment was conducted where the 6PIM load was varied, and voltages, currents and the rotating speed values were obtained at each operating point. The obtained voltage and speed (slip) values were used as inputs to the steady-state model. The supply voltage components in the dq and xy planes were maintained at $\hat{u}_{dqs} = 180$ V and $\hat{u}_{xys} = 16$ V, respectively. The dq voltage magnitude is higher than the rated magnitude ($\sqrt{2}U_{nf} = 168$ V), thereby insuring substantial saturation of the magnetic circuit. The selected value of the xy voltage component results in the xy plane current of approximately 70% of the rated value. Such test

© The Institution of Engineering and Technology 2015

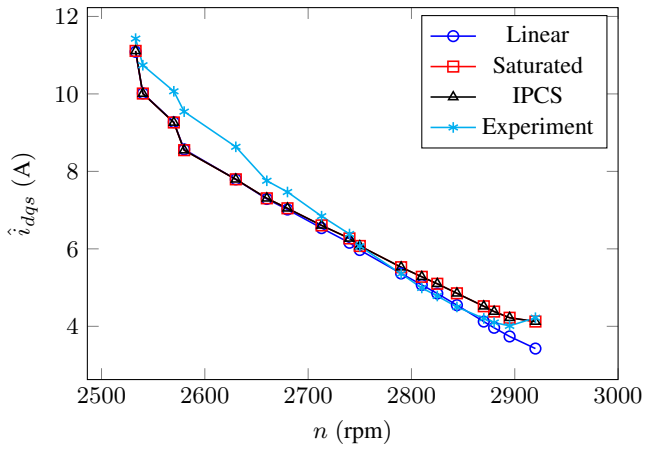

a

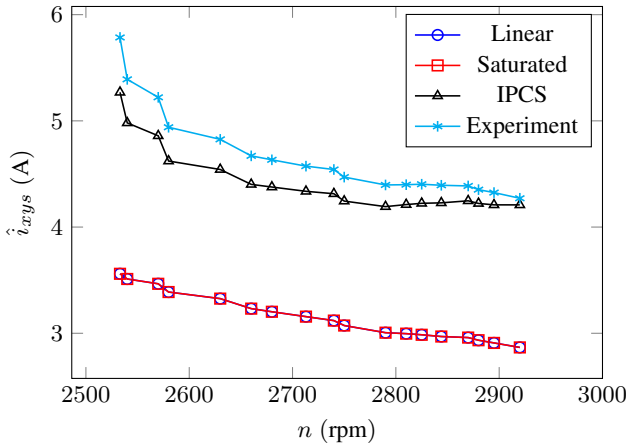

b

Fig. 8: Steady-state current magnitudes of the 6PIM obtained using the steady state model. The graphs display the variations of current magnitudes for different loading conditions
a dq plane current magnitude
b xy plane current magnitude

conditions are chosen in order to verify the model performance under heavy unbalance.

Values of dq and xy plane currents calculated from each model and the experimentally obtained values are plotted in Fig. 8. The dq current component calculated using the IPCS and saturated models shows better agreement with the experimental results compared to the linear model under light loads, where main flux saturation is the most pronounced. All three models exhibit an increased discrepancy between the measurements and calculated values under heavier loads, i.e. large slip values. This can be attributed to the non-linearity of the leakage inductance, which cannot be accounted for accurately enough using the Γ model. The xy current component calculated using the IPCS model is in much better agreement with the experimental values compared to the results of the linear and saturated models. Note that the values obtained using the linear and saturated models are identical, as the saturation effect in the xy plane is ignored altogether.

Steady state rms values of 6PIM phase currents are displayed in Fig. 9. Once again, the proposed IPCS model provides better agreement with the experimental results compared to the linear and saturated models. These results further emphasize the merits of the IPCS model. Note that the results of the linear model differ only slightly compared to the results of the saturated model. This is due to the fact that the linear model was formulated using the saturated (but constant) magnetizing inductance value, as previously stated. The

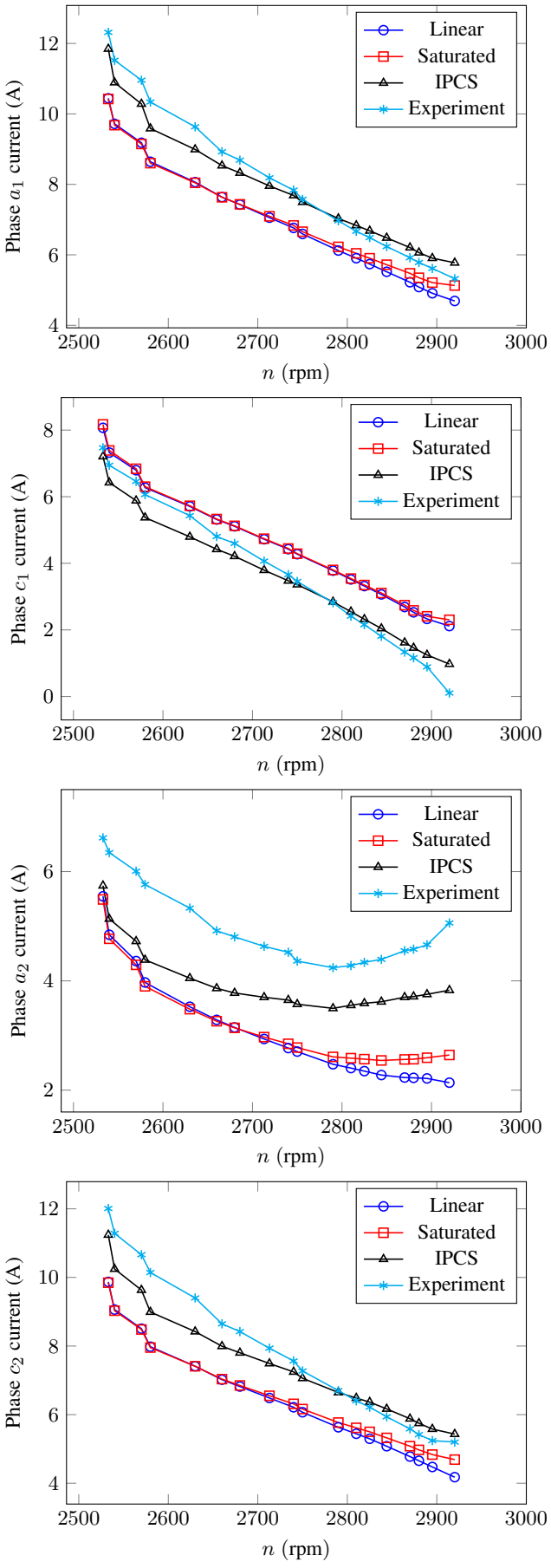

Fig. 9: Steady-state phase currents of the 6PIM (rms values) obtained using the steady state model. The graphs display the variations of current values for different loading conditions

© The Institution of Engineering and Technology 2015

traditional linear model which uses the unsaturated value of the magnetizing inductance would yield results which deviate significantly compared to the results of the saturated model.

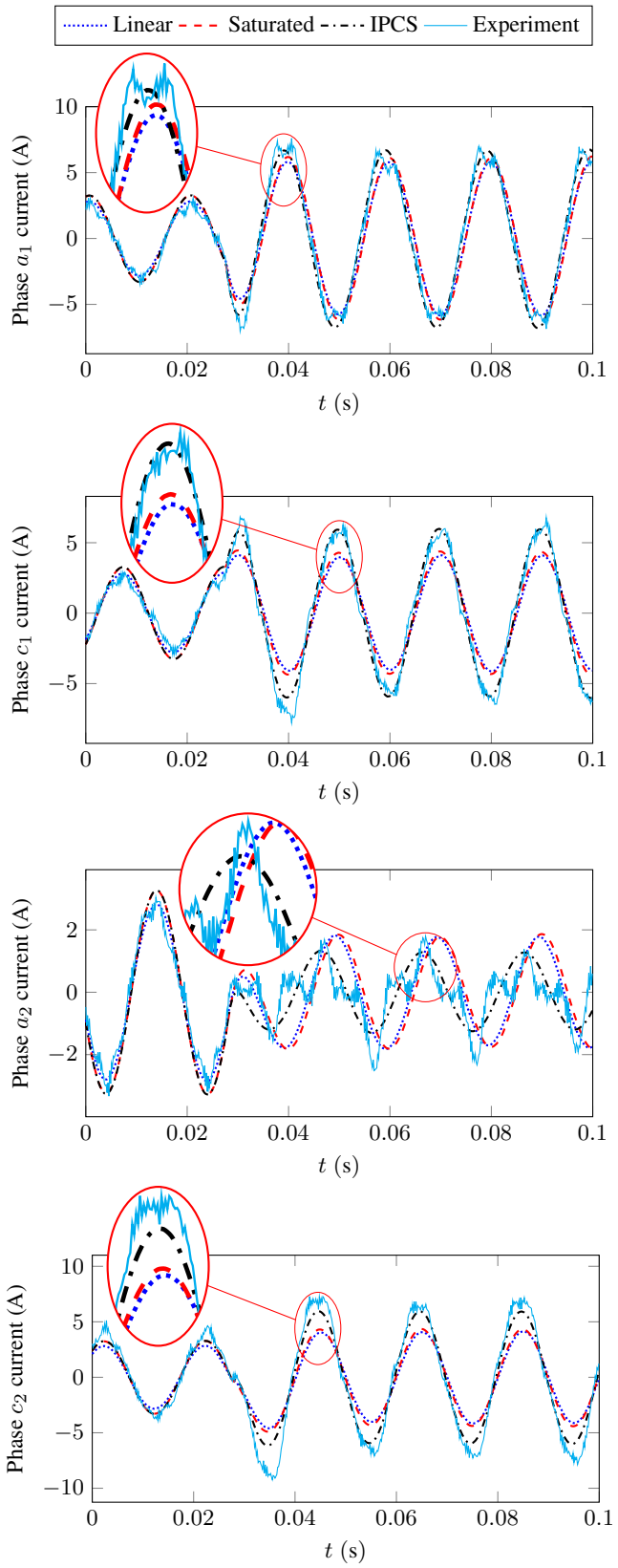

Fig. 10: Instantaneous values of 6PIM phase currents under a sudden change of the xy voltage component. The enlarged details emphasize the accuracy of the IPCS model

The performance of the dynamic model is demonstrated by performing a sudden increase of the xy voltage component. The experimentally obtained voltages are used as inputs to the dynamic model. Fig. 10 displays the calculated and experimentally obtained phase current waveforms. The increase in the xy voltage component occurs at $t = 28$ ms. The currents of the IPCS and saturated model are identical prior to the introduction of xy plane voltage, and are in good agreement with the experimental values. The linear model also provides a good approximation of experimental results under balanced supply, as it uses the values of magnetizing and leakage inductances corresponding to rated voltage and current, respectively. Following the voltage change, the IPCS model provides the most accurate results, both during the transient and in the new steady state. It should be noted that the currents obtained using the IPCS model best approximate the experimental results in terms of both phase and magnitude. The results of both the linear and saturated model deviate significantly from experimental results under unbalanced conditions.

The spectral analysis of experimental current waveforms reveals a presence of higher order harmonics, most notably the fifth and seventh. In a 6PIM, these components are projected into the xy plane [37]. As demonstrated in [12], the higher-order current harmonics in the xy subspace can be attributed to the air-gap flux distortion due to saturation. Another cause of low-order current harmonics is the inverter dead-time [35]. This effect is somewhat alleviated by the applied dead-time compensation. The presented research is aimed at analysing the fundamental frequency components of xy plane quantities, as stated in the Introduction. Therefore, the current distortion due to saturation and inverter dead-time was not accounted for.

6 Conclusion

A saturated VSD model of a 6PIM was presented. The model incorporated main and leakage flux saturation, as well as the mutual coupling between the dq and xy subspaces at the fundamental frequency. Fundamental frequency xy current components are not present in normal operation, but can be substantial in power sharing mode or in post-fault operation. The new model was aptly termed the IPCS model. The dq plane was modelled using the Γ model, similar to three-phase induction machines, which allowed determination of parameters directly from standard no-load and locked-rotor tests. An analysis of IPCS carried out using FEM revealed flux changes in the dq and xy plane. These flux changes were included in the flux-current relationships to account for the IPCS effect. An experimental method for determining the flux changes was proposed, and the obtained values were fitted using appropriate analytical functions. The IPCS model was then simulated in steady state and transient operating modes, under unbalanced supply conditions and with pronounced saturation. A comparison with the experimental results has demonstrated the advantages of the IPCS model compared to existing models.

Future research efforts will be aimed at improving the IPCS model by the inclusion of higher-order xy current harmonics inflicted by saturation. Specifically, in the case of 6PIM, the fifth and seventh harmonic should be included, as they are the most pronounced.

7 References

1 Levi, E., Barrero, F., Duran, M.J.: 'Multiphase machines and drives-revisited', *IEEE Transactions on Industrial Electronics*, 2016, **63**, (1), pp. 429–432

2 Subotic, I., Bodo, N., Levi, E.: 'Integration of six-phase EV drivetrains into battery charging process with direct grid connection', *IEEE Transactions on Energy Conversion*, 2017, **32**, (3), pp. 1012–1022

3 Rubino, S., Bojoi, R., Cavagnino, A., *et al.* 'Asymmetrical twelve-phase induction starter/generator for more electric engine in aircraft'. 2016 IEEE Energy Conversion Congress and Exposition (ECCE), Milwaukee, WI, 2016, pp. 1–8

4 Cao, W., Mecrow, B.C., Atkinson, G.J., *et al.*: 'Overview of electric motor technologies used for more electric aircraft (MEA)', *IEEE Transactions on Industrial Electronics*, 2012, **59**, (9), pp. 3523–3531

5 Chinmaya, K.A., Singh, G.K.: 'Performance evaluation of multiphase induction generator in stand-alone and grid-connected wind energy conversion system', *IET Renewable Power Generation*, 2018, **12**, (7), pp. 823–831

© The Institution of Engineering and Technology 2015

6 Levi, E., Bojoi, R., Profumo, F., *et al.*: 'Multiphase induction motor drives - a technology status review', *IET Electric Power Applications*, 2007, **1**, (4), pp. 489–516
7 Levi, E.: 'Multiphase electric machines for variable-speed applications', *IEEE Transactions on Industrial Electronics*, 2008, **55**, (5), pp. 1893–1909
8 Barrero, F., Duran, M.J.: 'Recent advances in the design, modeling, and control of multiphase machines-part i', *IEEE Transactions on Industrial Electronics*, 2016, **63**, (1), pp. 449–458
9 Levi, E. 'Multiphase ac machines'. Irwin, J.D., editor. The Industrial Electronics Handbook on Power Electronics and Motor Drives. (CRC Press, 2011. pp. 1–31)
10 Lipo, T.A. 'A d-q model for six phase induction machines'. International Conf. Electrical Machines, Athens, Greece, 1980,
11 Zhao, Y., Lipo, T.A.: 'Space vector PWM control of dual three-phase induction machine using vector space decomposition', *IEEE Transactions on Industry Applications*, 1995, **31**, (5), pp. 1100–1109
12 Abdel-Khalik, A.S., Ahmed, S., Elserougi, A.A., *et al.*: 'A voltage-behind-reactance model of five-phase induction machines considering the effect of magnetic saturation', *IEEE Transactions on Energy Conversion*, 2013, **28**, (3), pp. 576–592
13 Hofmann, H., Sanders, S.R., Sullivan, C.R.: 'Stator-flux-based vector control of induction machines in magnetic saturation', *IEEE Transactions on Industry Applications*, 1997, **33**, (4), pp. 935–942
14 Brown, J.E., Kovacs, K.P., Vas, P.: 'A method of including the effects of main flux path saturation in the generalized equations of a.c. machines', *IEEE Transactions on Power Apparatus and Systems*, 1983, **PAS-102**, (1), pp. 96–103
15 Vas, P., Brown, J.E., Hallenius, K.E.: 'Cross-saturation in smooth-air-gap electrical machines', *IEEE Transactions on Energy Conversion*, 1986, **EC-1**, (1), pp. 103–112
16 Marti, J.R., Louie, K.W.: 'A phase-domain synchronous generator model including saturation effects', *IEEE Transactions on Power Systems*, 1997, **12**, (1), pp. 222–229
17 Levi, E., Levi, V.A.: 'Impact of dynamic cross-saturation on accuracy of saturated synchronous machine models', *IEEE Transactions on Energy Conversion*, 2000, **15**, (2), pp. 224–230
18 Singh, G.K.: 'Modeling and experimental analysis of a self-excited six-phase induction generator for stand-alone renewable energy generation', *Renewable Energy*, 2008, **33**, (7), pp. 1605–1621
19 Jonsky, T., Stichweh, H., Theseling, M., *et al.* 'Modeling and parameter identification of multiphase permanent magnet synchronous motors including saturation effects'. 17th European Conference on Power Electronics and Applications, EPE-ECCE Europe, Geneva, Switzerland, 2015,
20 Amiri, N., Ebrahimi, S., Chapariha, M., *et al.*: 'Voltage-behind-reactance model of six-phase synchronous machines considering stator mutual leakage inductance and main flux saturation', *Electric Power Systems Research*, 2016, **138**, pp. 155–164
21 Amiri, N., Ebrahimi, S., Jatskevich, J., *et al.*: 'Saturable and decoupled constant-parameter vbr model for six-phase synchronous machines in state-variable simulation programs', *IEEE Transactions on Energy Conversion*, 2019, **34**, (4), pp. 1868–1880
22 Pereira, L.A., Scharlau, C.C., Pereira, L.F.A., *et al.*: 'Influence of saturation on the airgap induction waveform of five-phase induction machines', *IEEE Transactions on Energy Conversion*, 2012, **27**, (1), pp. 29–41
23 Che, H.S., Levi, E., Jones, M., *et al.*: 'Current control methods for an asymmetrical six-phase induction motor drive', *IEEE Transactions on Power Electronics*, 2014, **29**, (1), pp. 407–417
24 Zhou, C., Yang, G., Su, J.: 'Pwm strategy with minimum harmonic distortion for dual three-phase permanent-magnet synchronous motor drives operating in the overmodulation region', *IEEE Transactions on Power Electronics*, 2016, **31**, (2), pp. 1367–1380
25 González Prieto, I., Duran, M.J., Entrambasaguas, P., *et al.*: 'Field oriented control of multiphase drives with passive fault-tolerance', *IEEE Transactions on Industrial Electronics*, 2020, **67**, (9), pp. 7228–7238
26 Jecmenica, M., Brkovic, B., Levi, E., *et al.*: 'Interplane cross-saturation in multiphase machines', *IET Electric Power Applications*, 2019, **13**, (11), pp. 1812–1822
27 Duran, M.J., Prieto, I.G., Bermudez, M., *et al.*: 'Optimal Fault-Tolerant Control of Six-Phase Induction Motor Drives With Parallel Converters', *IEEE Transactions on Industrial Electronics*, 2016, **63**, (1), pp. 629–640
28 Zoric, I., Jones, M., Levi, E.: 'Arbitrary Power Sharing Among Three-Phase Winding Sets of Multiphase Machines', *IEEE Transactions on Industrial Electronics*, 2018, **65**, (2), pp. 1128–1139
29 Tani, A., Serra, G., Mengoni, M., *et al.* 'Dynamic stator current sharing in quadruple three-phase induction motor drives'. IECON 2013 - 39th Annual Conference of the IEEE Industrial Electronics Society, Vienna, Austria, 2013, pp. 5173–5178
30 Lyra, R.O.C., Lipo, T.A.: 'Torque density improvement in a six-phase induction motor with third harmonic current injection', *IEEE Transactions on Industry Applications*, 2002, **38**, (5), pp. 1351–1360
31 Stumberger, B., Stumberger, G., Hamler, A., *et al.*: 'Increasing of output power capability in a six-phase flux-weakened permanent magnet synchronous motor with a third harmonic current injection', *IEEE Transactions on Magnetics*, 2003, **39**, (5), pp. 3343–3345
32 Hadiouche, D., Razik, H., Rezzoug, A.: 'On the modeling and design of dual-stator windings to minimize circulating harmonic currents for VSI fed AC machines', *IEEE Transactions on Industry Applications*, 2004, **40**, (2), pp. 506–515
33 Slemon, G.R.: 'Modelling of induction machines for electric drives', *IEEE Transactions on Industry Applications*, 1989, **25**, (6), pp. 1126–1131
34 Che, H.S., Abdel-Khalik, A.S., Dordevic, O., *et al.*: 'Parameter estimation of asymmetrical six-phase induction machines using modified standard tests', *IEEE Transactions on Industrial Electronics*, 2017, **64**, (8), pp. 6075–6085
35 Vukosavic, S.: 'Grid-Side Converters Control and Design'. (Springer, 2018)
36 Boldea, I., Nasar, S.A.: 'The Induction Machine Handbook'. (CRC Press, 2002)
37 Klingshirn, E.A.: 'High phase order induction motors - part i-description and theoretical considerations', *IEEE Transactions on Power Apparatus and Systems*, 1983, **PAS-102**, (1), pp. 47–53

8 Appendix

8.1 6PIM rated data and design parameters

The rated data of the 6PIM are given in Table 2. The rated data are estimated based on the design parameters. To accurately determine the rated current and power, a thermal test would need to be conducted. Table 3 contains the main dimensions and winding information of the 6PIM. The machine dimensions are denoted in the cross-section shown in Fig. 11. The rotor bars were inaccessible for measurement, therefore the rotor slot dimensions were estimated based on an analytical procedure proposed in [36]. The stator winding is a two-layer full-pitch distributed winding with two slots per pole and phase, as shown in Fig. 12.

8.2 FE model of the 6PIM

The FE model of the 6PIM developed according to the design information of Table 3 is used in the analysis of section 4.1. The material properties and maximal mesh sizes of individual blocks are given in Table 4. The highest mesh density is used in the air-gap area, where most of the magnetic field strength is localized. The mesh in the iron part is coarser compared to the air-gap, but is still limited due to potentially high field strength in saturated conditions. Due to the low flux density in the stator and rotor slot areas, it was acceptable to allow the solver to determine the mesh sizes in these areas automatically. Note that the mesh generator automatically reduces the element size where needed, e.g., in the vicinity of boundaries, corners and arcs.

The cross-section of the FE model displaying the flux density distribution and the finite element mesh is given in Fig. 13. The displayed FE solution corresponds to the case where the main flux

Table 2 6PIM prototype rated data

Parameter	Designation	Value
Rated phase voltage	U_{nf}	119 V
Rated frequency	f_n	50 Hz
Rated current	I_n	3.19 A
Rated power	P_n	1410 W

Table 3 6PIM prototype design parameters

Parameter	Designation	Value
Stator outer diameter	D_{so}	125 mm
Rotor outer diameter	D_{ro}	64.3 mm
Rotor shaft diameter	D_{sh}	26 mm
Rotor inner diameter	D_{ri}	6.2 mm
Air-gap length	δ	0.35 mm
Stator yoke height	h_{ys}	17.5 mm
Rotor yoke height	h_{yr}	6.1 mm
Stator tooth height	h_{ts}	12.5 mm
Stator slot height	h_{ys}	10.7 mm
Stator slot width (inside)	w_{ss1}	5.2 mm
Stator slot width (outside)	w_{ss2}	6.9 mm
Stator slot opening width	w_{bs}	2.2 mm
Stator slot opening height	h_{bs}	0.6 mm
Axial length	l_a	90 mm
No. of stator slots	Q_s	24
No. of rotor slots	Q_r	28
No. of pole pairs	p	1
Stator winding connection	/	Y
Turns per phase	N_{ph}	104
Winding type	/	two-layer
Winding pitch	y	12

© The Institution of Engineering and Technology 2015

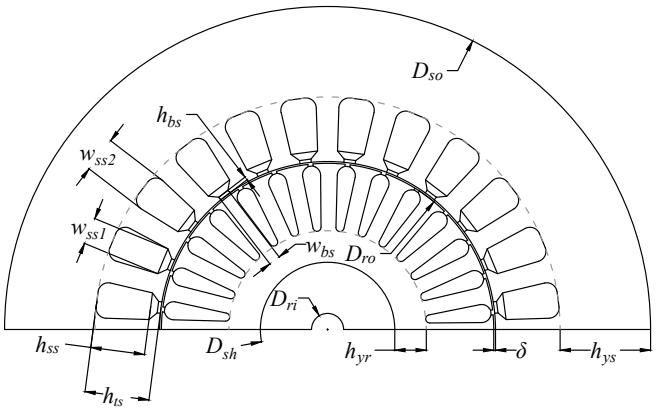

Fig. 11: Cross-section of the 6PIM magnetic circuit with the main dimensions denoted

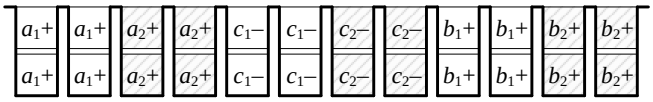

Fig. 12: Schematic display of the stator winding spanning one pole pitch. The $+$ and $-$ signs indicate the direction of the coil sides

Table 4 Material properties and maximal mesh sizes of FEM block: M-19 Steel – laminated non-oriented steel, 1010 Steel – solid steel

Machine part	Material	Mesh size
Stator magnetic circuit	M-19 Steel	1 mm
Rotor magnetic circuit	M-19 Steel	1 mm
Rotor shaft	1010 Steel	1 mm
Stator winding	Copper (⌀ 0.75 mm)	Auto
Rotor bars	Aluminium	Auto
Air-gap	Air	0.05 mm

saturation and IPCS are both highly pronounced. The FE simulation was conducted using 85000 nodes (168990 elements). The mesh in the air-gap area is shown in the enlarged detail of Fig. 13. To prove the accuracy of the results obtained using the selected mesh size, the mesh in the air-gap and the iron parts of the machine was refined, increasing the number of nodes to 190000. This modification resulted in an increase in accuracy of no more than 0.2% in terms of per-phase flux linkages, thus proving that the selected mesh density guarantees satisfying accuracy.

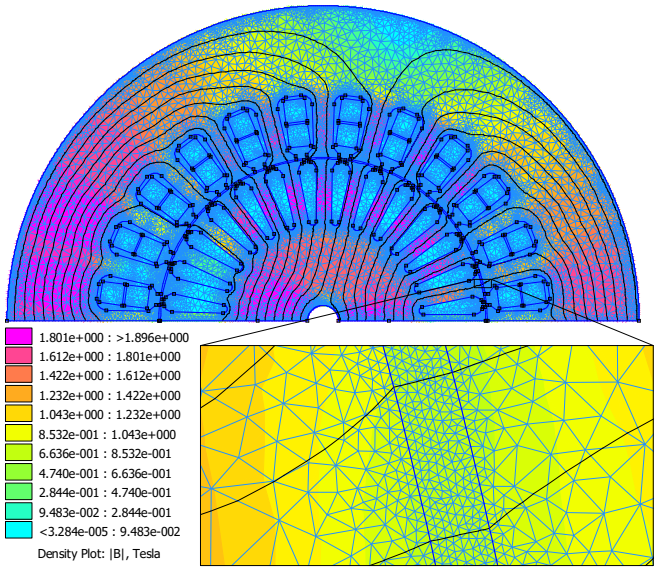

Fig. 13: Solution of 6PIM analysis in the FEA software for ($\hat{i}_M = 6$ A, $\hat{i}_{xys} = 6$ A) with the flux density distribution and mesh displayed. The enlarged detail shows the air-gap mesh

8.3 Non-linear model parameters

The dq subspace leakage inductance is given as a two-segment non-linear function of the stator current in (19). As noted, expressing the leakage inductance solely as the function of stator current is suggested in [33]. The dq flux change is expressed as a two-segment non-linear function of the magnetizing current in (20). The influence of IPCS on the dq flux change, albeit present, is negligible from a practical standpoint. The dq flux change is therefore expressed in terms of the magnetizing current alone, disregarding the influence of the xy current component. The flux change in the xy plane is expressed by (21), as a two-dimensional function of the magnetizing and xy plane currents. The values of constant parameters L_{Lu} and L_{Mu} featured in (19) and (20) are given in Table 1.

$$L_L(\text{mH}) = \begin{cases} L_{Lu}, & \hat{i}_{dqs} < 0.057 \text{ A} \\ -0.5219 \cdot \hat{i}_{dqs}^{-2} + 17.52 \cdot \hat{i}_{dqs}^{-1} + 11.37 - 0.2121 \cdot \hat{i}_{dqs}, & \hat{i}_{dqs} \geq 0.057 \text{ A} \end{cases} \tag{19}$$

$$\Delta\psi'_{dq}(\text{Wb}) = \begin{cases} 0, & \hat{i}_M < 0.679 \text{ A} \\ \left(1.242 + 1.691 \cdot \hat{i}_M^{-1} + 0.5723 \cdot \hat{i}_M^{-2}\right)^{-1} - L_{Mu}\hat{i}_M, & \hat{i}_M \geq 0.679 \text{ A} \end{cases} \tag{20}$$

$$\Delta\psi'_{xy}(\text{Wb}) = -\left(5.56 \cdot \hat{i}_{xys} + 0.6733 \cdot \hat{i}_{xys}^2\right) \cdot \left(4.168 + 1.787 \cdot \hat{i}_M - 0.0516 \cdot \hat{i}_M^2\right) \cdot 10^{-2} \tag{21}$$

© The Institution of Engineering and Technology 2015